Nano Research

Open Access

Research Article

NbO_6 octahedra of high-dimensional Nb_2O_5 boosting H_2O_2 electrosynthesis for sewage pollutants degradation

Bingxue Cheng[1], Xinlin Wang[1], Shijia Li[2], Yuhang Li[2], Toru Murayama[3], Tamao Ishida[4,5] ✉, Guangli Xiu[1], Kenji Iida[3], Yufan Fu[1], Yining Wang[1], and Mingyue Lin[1] ✉

[1] *State Environmental Protection Key Laboratory of Environmental Risk Assessment and Control on Chemical Process, Shanghai Environmental Protection Key Laboratory on Environmental Standard and Risk Management of Chemical Pollutants, School of Resources and Environmental Engineering, East China University of Science and Technology, Shanghai 200237, China*
[2] *School of Materials Science and Engineering, East China University of Science and Technology, Shanghai 200237, China*
[3] *Institute for Catalysis, Hokkaido University, Kita21, Nishi10, Kita-ku, Sapporo, Hokkaido 001-0021, Japan*
[4] *Research Center for Artificial Photosynthesis (ReCAP), Osaka Metropolitan University, 3-3-138 Sugimoto, Sumiyoshi-ku, Osaka 558–8585, Japan*
[5] *Department of Chemistry and Bioengineering, Graduate School of Engineering, Osaka Metropolitan University, 3-3-138 Sugimoto, Sumiyoshi-ku, Osaka 558–8585, Japan*

Cite this article: *Nano Research*, **2025**, *18*, 94907917. https://doi.org/10.26599/NR.2025.94907917

ABSTRACT: Two-electron oxygen reduction reaction (2e⁻ ORR) to produce hydrogen peroxide (H_2O_2) presents an efficient, secure, and sustainable method. However, the competing four-electron pathway produces H_2O, yielding low H_2O_2 selectivity (~ 70%). In this work, a high-dimensional rod-like structure of niobium oxide (Nb_2O_5-HD) containing NbO_6 octahedra was synthesized using a hydrothermal method combined with a calcination strategy. Under 50 mA·cm^{-2}, the Faradaic efficiency (FE) of H_2O_2 reached 94%, with the H_2O_2 yield reaching as high as 874 mmol·g_{cat}^{-1}·h^{-1}. After 34 h of operation, FE was still 76%, and the stability is great. *In situ* Raman spectroscopy analysis and experiments revealed that the NbO_6 octahedra on Nb_2O_5-HD were the key factor for its excellent ORR activity and H_2O_2 FE. This inspires the development of high-performance ORR transition metal electrocatalysts.

KEYWORDS: oxygen reduction reaction, niobium oxide, hydrogen peroxide, pollutant degradation

1 Introduction

Hydrogen peroxide (H_2O_2) functions as a commonly utilized oxidant across diverse industrial sectors, including papermaking, wastewater treatment [1, 2], and disinfection [3]. The industrial synthesis of H_2O_2 primarily relies on the oxidation–reduction reaction of anthraquinone. However, this process demands high investment, involves complex process flows, and may contribute to environmental pollution due to the use of organic solvents. Alternatively, producing H_2O_2 via the electrocatalytic oxygen reduction reaction (ORR) offers a simpler, less capital-intensive, safer, and environmentally friendly approach. The ORR pathway for H_2O_2 production entails the transfer of two electrons and faces two primary challenges: (i) the sluggish kinetics of ORR, which necessitates operation at a significant overpotential; (ii) the preferential 4e⁻ pathway of ORR towards H_2O production, leading to lower energy efficiency and selectivity (~ 70%) in the electrosynthesis of H_2O_2 [4]. Therefore, exploring electrocatalysis with high activity and selectivity is crucial for the industrial electrosynthesis of H_2O_2.

Compared to noble metal materials and single-atom catalysts, transition metal oxide electrocatalysts have garnered extensive research attention due to their affordability and environmental compatibility. In particular, ZnO exhibits a remarkable selectivity of 90.0% for H_2O_2 and demonstrates exceptional performance and stability with a stable production rate of 211.94 mmol·g_{cat}^{-1}·h^{-1} throughout prolonged stability tests [5]. Similarly, niobium pentoxide (Nb_2O_5), another transition metal oxide, displays outstanding optical and electrochemical properties, showing great potential in electrochemistry [6]. It is noteworthy that Nb_2O_5 exhibits diverse crystalline phases, including amorphous (A) and

Received: May 22, 2025
Accepted: August 12, 2025

✉Address correspondence to Tamao Ishida, tishida@omu.ac.jp; Mingyue Lin, ms.mingyuelin@ecust.edu.cn

orthorhombic (T) phases, with the transformation of these phases depending on the calcination temperature [7]. Studies have indicated that monoclinic Nb_2O_5 can achieve an H_2O_2 Faraday efficiency (FE) of approximately 70%, and this FE can be further enhanced to 93.4% by employing specific calcination strategies to increase oxygen vacancies on the material's surface [8]. Additionally, pseudo-hexagonal Nb_2O_5 also exhibits an H_2O_2 FE of approximately 86% [9]. Consequently, Nb_2O_5 materials exhibit excellent performance in ORR.

In this work, we prepared a high-dimensional structure of niobium oxide (Nb_2O_5-HD) through hydrothermal synthesis and calcination processes. Electrochemical test results revealed that Nb_2O_5-HD attained 58 mA·cm^{-2} at 0.4 V vs. RHE. At 50 mA·cm^{-2}, the FE of H_2O_2 reached 94%, corresponding to 874 mmol·g_{cat}^{-1}·h^{-1} of H_2O_2 productivity. After 34 h of operation, FE was still 76%, and the stability is great. This performance is significantly better than that of conventional catalysts for the electrosynthesis of H_2O_2. After a thorough analysis of its catalytic mechanism, it has been discovered that the NbO_6 octahedra are the key factor for the excellent electrocatalytic performance.

2 Experimental section

2.1 Catalysts preparation

Nb_2O_5-HD was synthesized through a hydrothermal process, employing ammonium niobium oxalate ($NH_4[NbO(C_2O_4)_2(H_2O)_2]\cdot nH_2O$, Sigma-Aldrich) as the starting material. The ammonium niobium oxalate was combined with deionized water, followed by hydrothermal treatment at 175 °C for 24 h. The reaction-generated solid was cleaned using deionized water and dried at 60 °C for a period extending through one night. The dry, white powder was then calcined at 400 °C for 2 h to yield the final Nb_2O_5-HD powder. Amorphous Nb_2O_5 (Nb_2O_5-A) was synthesized from JRC-NbO-1 ($Nb_2O_5\cdot nH_2O$, purchased from Japan Catalytic Association) by calcining at 400 °C for 2 h. The synthesis method for orthorhombic Nb_2O_5 (T-Nb_2O_5) is the same as that of Nb_2O_5-HD, but the calcination temperature is 650 °C.

Working electrode materials were prepared for subsequent electrocatalytic performance testing. To formulate the catalyst ink, 10 mg of catalyst powder was combined with 960 μL of ethanol and 40 μL of Nafion solution. Following this, the mixed suspension was sonicated for 30 min. Then, 100 μL of the resulting ink was taken and evenly drop-coated on 1 cm × 1 cm carbon paper (CP, SGL Sigracet 28BC), which was later illuminated dry with an infrared lamp. The prepared Nb_2O_5-HD/CP catalyst was used for subsequent electrocatalytic tests.

2.2 Catalyst morphology characterization

The scanning electron microscopy (SEM) images were acquired using ZEISS Gemini SEM 300 operated at 3 kV. Transmission electron microscope (TEM) characterization employed a JEOL JEM-2100 F instrument for image acquisition.

The powder X-ray diffraction (XRD) was performed on a Rigaku Smartlab SE instrument, utilizing Cu-Kα_1 radiation with a wavelength of 0.1541 Å and a scan rate of 5 °·min^{-1}. The X-ray photoelectron spectra (XPS) were recorded on Thermo Scientific K-Alpha by using Al Kα radiation ($h\nu$ = 1486.6 eV). Before the analysis, all XPS data were corrected with the adventitious C 1s signal at 284.8 eV.

2.3 *In situ* Raman spectroscopy

In situ Raman spectroscopy analysis was carried out using a Horiba LABRAM HR Raman spectrometer. For these *in situ* experiments, specifically designed electrochemical cells are employed, incorporating nickel foam as the counter electrode and Ag/AgCl serving as the reference electrode. A 532 nm excitation wavelength was applied, with measurements performed via a microscopic objective lens characterized by 50× magnification and a numerical aperture of 0.55.

2.4 Actual H_2O_2 production measurement

A homemade flow-through electrolytic cell was used to measure the actual H_2O_2 production. It consists of cathode and anode chambers and a venting chamber. The electrolyte was 1 M KOH. A Nafion 117 membrane is sandwiched between the cathode and anode chambers, with the side of the catalyst-covered carbon paper near the cathode. Rubber gaskets were placed between the chambers to make the device leak-free. The rate of flow for the electrolyte was set at 10 mL·min^{-1}, while the O_2 flow rate was maintained at 8 mL·min^{-1}.

The determination of H_2O_2 concentration by cerium sulfate titration is based on the principle that the yellow Ce^{4+} solution will be reduced to colorless Ce^{3+} by H_2O_2. Take 2 mL of the catholyte after the reaction, add 10 mL of 0.5 mol H_2SO_4, and titrate with 0.02 mol of $Ce(SO_4)_2$ solution. The concentration of the sample can be obtained based on the linear correlation between the $Ce(SO_4)_2$ concentration and the H_2O_2 concentration.

2.5 Pollutant degradation testing

The typical water-soluble organic pollutant, methylene blue (MB), was selected as the target degradation agent, and 10 mg·L^{-1} MB aqueous solution was prepared. During the degradation process, H_2O_2 was added directly into the MB solution while stirring was maintained continuously. The samples were collected every 10 min, and the spectrophotometer (model 722 G) was used to measure the absorbance changes of these samples at 665 nm.

3 Results and discussion

3.1 Analysis of catalyst properties

Firstly, the crystal structure and phase composition of the material were examined by XRD. The XRD pattern showed two peaks at 2θ = 22.8° and 46.4° (Fig. S1(a) in the Electronic Supplementary Material (ESM)). Based on relevant literature, several studies have reported XRD characteristic peaks at 2θ = 22°–23° and 46°–47° for several metal oxides synthesized by the same hydrothermal method [10–13]. Thus, the 2θ = 22.8° and 46.4° diffraction peaks of Nb_2O_5-HD obtained by the hydrothermal synthesis were assigned to the (001) and (002) planes, respectively [10]. The lattice spacing of the (001) plane was calculated to be 3.91 Å, which was consistent with the length of the [NbO_6] octahedra structure in Nb_2O_5, indicating that the NbO_6-based polymorph was formed.

The reported materials above [10–13] develop rod-like crystal structures through octahedral stacking in the *c*-axis direction, with their rod-like crystal cross-sections constituted by a random configuration of pentagonal units (PUs) and [MO_6] octahedra. Therefore, these catalysts are referred to as high-dimensional structural oxides (HDS-oxides). In view of this, we conjecture that the synthesized materials are high-dimensional structures, but

further verification is still needed. Thus, to further confirm the structure of Nb_2O_5, Raman spectroscopy was conducted. As shown in Fig. S1(b) in the ESM, Nb_2O_5-HD exhibited a wide spectral band approximately at 700 cm^{-1}, which was associated with the symmetric stretching vibration of the NbO_6 octahedra [14]. The weak shoulder bands observed near 990 cm^{-1} could be ascribed to the symmetric stretching mode of the Nb=O surface [10], whereas the Raman bands located in the 200–300 cm^{-1} were linked to the bending mode of the Nb–O–Nb bond [15, 16].

SEM and TEM images were additionally performed to conduct detailed examinations of the material's microstructural features and morphological characteristics. The results showed that Nb_2O_5-HD was composed of nanorods aggregated into a cluster structure (Fig. 1(a) and Figs. S2(a) and S2(b) in the ESM). Statistically, these nanorods have an approximate diameter of 12 nm, with lengths ranging between 40 and 150 nm (Fig. S3 in the ESM). Estimated by the TEM images, two crystalline facets were identified with lattice spacings of 4.00 and 1.90 Å, respectively (Fig. 1(b)), which are consistent with the XRD patterns. The high-angle annular dark-field scanning transmission electron microscopy (HAADF-STEM) image showed the atomic arrangement of the rod-like cross-sections (Fig. S2(c) in the ESM). We can accordingly find PUs and octahedral randomly arranged structures, so we can determine that the synthesized Nb_2O_5 is a high-dimensional structure. Figure 1(c) shows the plausible structure of Nb_2O_5-HD, exhibiting a layered configuration comprising NbO_6 octahedra and NbO_7 pentagonal bipyramids interconnected within the *a*–*b* plane. The (001) diffraction corresponds to a hierarchical structure in the *c*-direction [10].

In addition, we confirmed the surface composition and valence state of Nb_2O_5-HD by XPS. The Nb 3d XPS peaks of Nb_2O_5-HD were located at 206.88 and 209.58 eV (Fig. S1(c) in the ESM), which corresponded to the Nb $3d_{5/2}$ and Nb $3d_{3/2}$ energy levels, respectively, indicating that Nb in Nb_2O_5-HD exists in the pentavalent state (Nb^{5+}). The O 1s spectra of Nb_2O_5-HD could be decomposed into three independent peaks at the binding energies of 530.9, 532.1, and 533.3 eV (Fig. S1(d) in the ESM). These peaks are attributed to lattice oxygens (O_L), oxygen vacancies (O_V), and adsorbed oxygen (O_A), respectively [17]. The above results illustrate the successful synthesis of high-dimensional niobium oxide.

Moreover, we also designed an amorphous Nb_2O_5 (Nb_2O_5-A) with a lesser amount of NbO_6 octahedra content. According to the Raman spectral analysis, the characteristic NbO_6 vibration mode in Nb_2O_5-HD was much stronger than that of Nb_2O_5-A (Fig. S4(a) in the ESM). The amorphous structure of Nb_2O_5-A is evidenced by its XRD pattern featuring a broad diffraction feature at $2\theta = 25°$ (Fig. S4(b) in the ESM), consistent with TEM/HAADF-STEM images showing no discernible lattice fringes (Fig. S5 in the ESM). All the above results verify the amorphous structure of this Nb_2O_5.

3.2 Evaluation of 2e⁻ ORR electrochemical performance

To evaluate the electrocatalytic performance of Nb_2O_5-HD/CP in the ORR process, we conducted a standard three-electrode configuration using an H-type electrolytic cell under ambient conditions (25 ± 1 °C, 1 atm) (Fig. 2(a)). As evidenced by linear sweep voltammetry (LSV) measurements, Nb_2O_5-HD/CP exhibited remarkable catalytic activity with a current density of 58 $mA{\cdot}cm^{-2}$ at 0.4 V vs. RHE, substantially exceeding the 3 $mA{\cdot}cm^{-2}$ recorded for bare CP (Fig. S6 in the ESM). This indicates that the contribution of CP substrate to the ORR process is negligible. The current density of Nb_2O_5-A was 15 $mA{\cdot}cm^{-2}$ lower than that of Nb_2O_5-HD at 0.4 V vs. RHE.

Further electrochemical characterization by cyclic voltammetry (CV) showed the double-layer capacitance (C_{dl}) value of 4.22 $mF{\cdot}cm^{-2}$ for Nb_2O_5-HD/CP, 3.73 $mF{\cdot}cm^{-2}$ for Nb_2O_5-A/CP, and 1.69 $mF{\cdot}cm^{-2}$ for the bare CP (Fig. 2(c) and Fig. S7 in the ESM). Since C_{dl} is proportional to the electrochemically active surface area (ECSA) [18], to exclude the effect of surface area on intrinsic activity, we calculated the ECSA using the C_{dl} method and normalized the LSV data accordingly. The ECSA of Nb_2O_5-HD/CP was calculated to be 105.5 cm^2, and that of the Nb_2O_5-A/CP to be 93.25 cm^2. The ECSA-normalized LSV plots revealed that Nb_2O_5 deposition notably boosted catalytic activity, with Nb_2O_5-HD (featuring a higher density of NbO_6 octahedra) demonstrating a more substantial enhancement in ORR activity (Fig. 2(d)). To further evaluate the reaction kinetics in ORR, the corresponding Tafel slopes were calculated (Fig. 2(e)). The Tafel slope of Nb_2O_5-HD/CP is 49.3 $mV{\cdot}dec^{-1}$, which is lower than that of Nb_2O_5-A/CP (62.9 $mV{\cdot}dec^{-1}$), indicating that NbO_6 octahedra in Nb_2O_5 are mainly responsible for the high ORR activity.

3.3 Assessment of actual H_2O_2 production

To quantitatively evaluate the actual ability of Nb_2O_5-HD catalyst to generate H_2O_2 under industrial-related conditions, we performed chronopotentiometry (CP) tests in a continuous electrolyte circulation (1 M KOH) flow cell (Fig. 2(b)). Firstly, we prepared catalysts with different loadings (0.5, 1, and 2 $mg{\cdot}cm^{-2}$), and their product yields and FEs were evaluated following 0.5 and 2 h ORR processes (Fig. S8 in the ESM). Under catalyst loadings of 0.5 and 1 $mg{\cdot}cm^{-2}$, the difference between H_2O_2 yield and FE was small after 0.5 h of ORR. With the reaction time increasing to 2 h, the H_2O_2 yield and FE of the catalyst with 0.5 $mg{\cdot}cm^{-2}$ loading (920 to 818 $mmol{\cdot}h^{-1}$, 99% to 88%) decreased faster than that of the catalyst with 1 $mg{\cdot}cm^{-2}$ (874 to 835 $mmol{\cdot}h^{-1}$, 94% to 90%) loading. As the

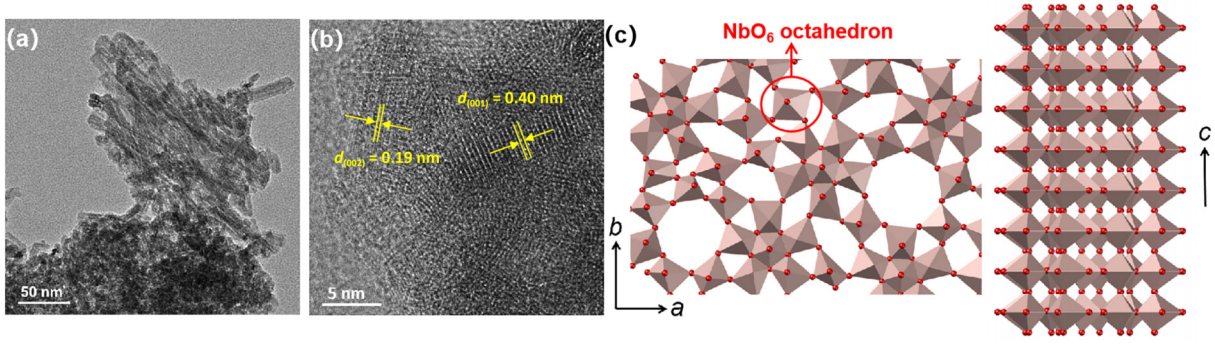

Figure 1 Structure characterization of the catalysts. (a) and (b) TEM images of Nb_2O_5-HD. (c) A plausible schematic structure of Nb_2O_5-HD.

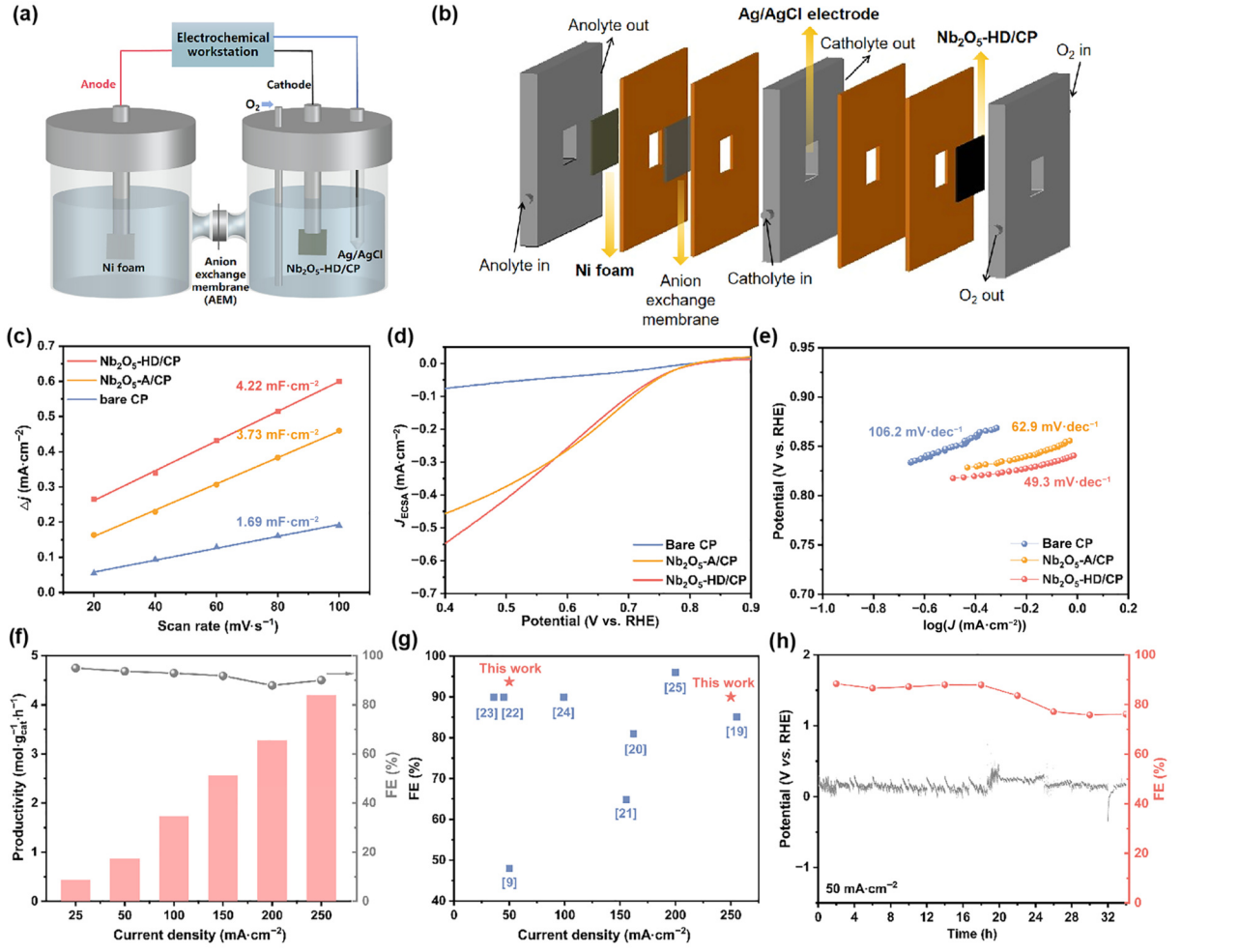

Figure 2 (a) Schematic structure of the H-type electrolytic cell. (b) Schematic structure of the flow cell. (c) Average capacitive current density of Nb_2O_5-HD/CP, Nb_2O_5-A/CP, and bare CP at different scan rates. (d) The ECSA–normalized LSV curves of Nb_2O_5-HD/CP, Nb_2O_5-A/CP, and bare CP in 1 M KOH. (e) Tafel plots of Nb_2O_5-HD/CP, Nb_2O_5-A/CP, and bare CP. (f) Productivity and FE of Nb_2O_5-HD for H_2O_2 generation at different current densities for 0.5 h ORR. (g) FE of H_2O_2 production of Nb_2O_5-HD compared to the reported electrocatalysts. (h) Stability test of Nb_2O_5-HD catalyst under 50 mA·cm^{-2}.

loading increased to 2 mg·cm^{-2}, both FE and yield decreased significantly. This may be due to the thicker catalyst load, resulting in less exposure of the active sites. Therefore, the catalyst loading of 1 mg·cm^{-2} was finally selected for the following electrochemical tests. Nb_2O_5-HD exhibited good catalytic activity, maintaining stability at high current densities. It is worth noting that within the current density range spanning from 25 to 250 mA·cm^{-2}, the FE for H_2O_2 production could be maintained at approximately 90%, reaching an FE of 94% at 50 mA·cm^{-2}, and the H_2O_2 production rate reached 874 mmol·g_{cat}^{-1}·h^{-1} (Fig. 2(f)). Nb_2O_5-HD exhibited excellent performance in H_2O_2 generation (Fig. 2(g)), surpassing many recently reported electrocatalytic H_2O_2 production catalysts (Table S1 in the ESM) [9, 19–25]. Then we performed stability tests at distinct current densities (10, 50, and 100 mA·cm^{-2}) and simultaneously observed the changes in FE. To eliminate the effect of H_2O_2, which is easily decomposed for a long time, we changed the electrolyte every 2 h. As shown in Fig. S9 in the ESM, under 10 mA·cm^{-2}, the 8 h CP curve was smooth, with FE sustaining 84%, but the yield of 8 h was only 156.8 mol·g_{cat}^{-1}·h^{-1}. While under 100 mA·cm^{-2}, we observed that the CP curve became undulating, and the FE decreased rapidly, to only 71.9% after 4 h. Therefore, we chose to perform a longer stability test at 50 mA·cm^{-2}. The catalyst worked stably for up to 34 h under these conditions, with the FE still maintained at 76% (Fig. 2(h)), the H_2O_2 selectivity remaining above 85%, and the yield also reaching 710 mmol·g_{cat}^{-1}·h^{-1} (Fig. S10 in the ESM). The above results showed that Nb_2O_5-HD has good ORR stability.

3.4 Catalytic mechanism investigation

The interfacial reactions on the catalyst during the ORR were investigated by comparing the XRD and XPS results before and after the reaction. The binding energy of elemental niobium experienced only a minor shift, which is negligible, after the ORR reaction (Fig. 3(a)). This suggests that niobium maintained a stable oxidation state during the ORR process without undergoing substantial chemical transformation or degradation. Compared to the unreacted Nb_2O_5-HD, the O 1s peaks changed significantly, and the peaks of O_A disappeared, indicating that all the adsorbed oxygen originally present on the substance participated in the reaction. The presence of O_V contributes to the creation of additional active sites, enabling reactant interaction and thereby facilitating the electrocatalytic reaction [26]. It can be found that the O_V/O_L value after the reaction (0.17) is much smaller than that before the reaction (0.41) (Fig. 3(b)), and the O 1s peak shifted toward a lower binding energy. These results collectively demonstrate the presence of abundant oxygen vacancies on Nb_2O_5-

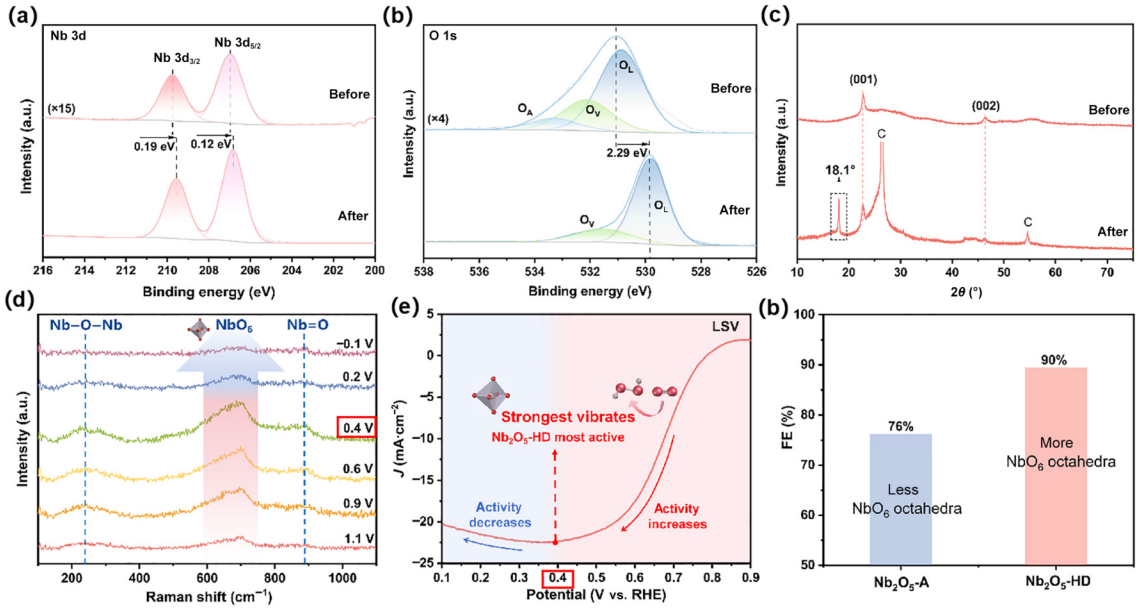

Figure 3 (a) Nb 3d and (b) O 1s XPS spectra of Nb_2O_5-HD in the ORR. (c) The XRD patterns of Nb_2O_5-HD before and after ORR reaction. (d) *In situ* Raman spectra of Nb_2O_5-HD in 1 M KOH during ORR. (e) LSV curve of Nb_2O_5-HD. (f) FE of H_2O_2 after 2 h ORR on Nb_2O_5-HD and Nb_2O_5-A.

HD before the reaction, which is favorable for the electrocatalytic reaction.

Comparing the XRD patterns before and after the reaction, it can be found that the intensity of the peak at 2θ = 46.4° is weakened after the reaction, while new peaks appeared at 2θ = 18.1, 26.5, and 54.3°. It is noteworthy that the narrow, sharp peaks at 2θ = 26.5 and 54.3° belonged to the carbon peaks. The new peak at 18.1° matches the peak at the (060) crystal face of orthorhombic phase Nb_2O_5 (JCPDS No. 30-0873). This indicates that the crystalline structure of the Nb_2O_5-HD is involved in the ORR, and the surface structure of the Nb_2O_5 catalysts changes during the ORR process (Fig. 3(c)).

In situ Raman spectroscopy analysis was conducted to further determine the dynamic behavior of Nb_2O_5-HD during the ORR process (Fig. 3(d)). As the applied voltage decreases from 1.1 to 0.4 V vs. RHE, a gradual increase in the intensity of the Raman peaks situated near 200, 700, and 890 cm^{-1} was noticed, especially the significant change in the broadband centered at 700 cm^{-1}, which was ascribed to the symmetric stretching mode of the NbO_6 octahedra. The corresponding LSV plots of the Nb_2O_5-HD showed an enhancement in catalytic activity during this process (Fig. 3(e)). However, when the voltage was further reduced, the intensity of these three peaks decreased rapidly, accompanied by a decrease in catalytic activity. The above results suggested that the NbO_6 octahedra may be the ORR active site.

The difference between different crystal types of Nb_2O_5 is the amount of NbO_6 octahedra on the shear surface [27]. Therefore, we used the performance comparison of Nb_2O_5 with different NbO_6 octahedra contents to verify the proposed relationship between NbO_6 octahedra and ORR performance. Firstly, from the data of electrochemical performance evaluation, Nb_2O_5-A with fewer NbO_6 octahedra has poorer ORR activity than Nb_2O_5-HD, and the kinetics of the reaction is slower (Figs. 2(c)–2(e)). And the CP results showed that the H_2O_2 FE of Nb_2O_5-A with fewer NbO_6 octahedra was also 14% lower than that of Nb_2O_5-HD (Fig. 3(f)). In addition, orthorhombic niobium oxide (T-Nb_2O_5) with more NbO_6 octahedra was further prepared and was found to have higher H_2O_2 FE and better stability than Nb_2O_5-HD (Fig. S11 in the ESM). The above results strongly confirm the importance of NbO_6 octahedra in improving the ORR activity and H_2O_2 FE of Nb_2O_5.

The vibration of the NbO_6 octahedra affects the changes in the crystalline surface, so we further observed the sample morphology to elucidate the changes in the crystal structure of the catalyst. The SEM image showed that its nanorod structure (Fig. S12(a) in the ESM) and the spacing of the (001) crystalline plane remained unchanged after the ORR reaction of Nb_2O_5-HD. However, the (002) lattice fringes became relatively blurred, and a new crystal spacing of 0.48 nm appeared (Fig. S12(b) in the ESM). This newly emerged lattice spacing coincides perfectly with the new peak observed at 2θ = 18.1° in the XRD pattern. These results strongly suggest that the structure of Nb_2O_5-HD has changed on the (002) crystal plane (i.e., the *a*–*b* plane) during the ORR process due to the vibration of the NbO_6 octahedra.

According to the above experimental and structural characterization results, the NbO_6 octahedra in Nb_2O_5-HD are confirmed to be the key factor for its high ORR activity and H_2O_2 FE.

3.5 Application to pollutant degradation

The present study also endeavors to explore the potential of H_2O_2 generated through ORR for practical applications in pollutant degradation (Fig. 4(a)). The ORR was performed at 50 mA·cm^{-2} for 2 h. The generated H_2O_2 was collected, and its concentration was accurately determined by titration to be 39.6 mmol·L^{-1}. Subsequently, 1 mL of the generated H_2O_2 was introduced into 30 mL of MB solution and continuously agitated at ambient temperature. The molar ratio of MB and H_2O_2 was 1:40. After 90 min of reaction with H_2O_2 addition, the MB aqueous solution achieved a decolorization percentage of 23.72% (Fig. 4(b)), and the degradation rate constant was calculated to be 0.0034 (Fig. 4(c)), which is slightly more efficient than the treatment of MB with H_2O_2 only in other studies (Fig. 4(d)). Upon raising the molar ratio of MB to H_2O_2 to 1:1200, the MB aqueous solution exhibited a decolorization efficiency of 75.81% following a 90-minute reaction period (Fig. S13 in the ESM). This verifies the high applicability of

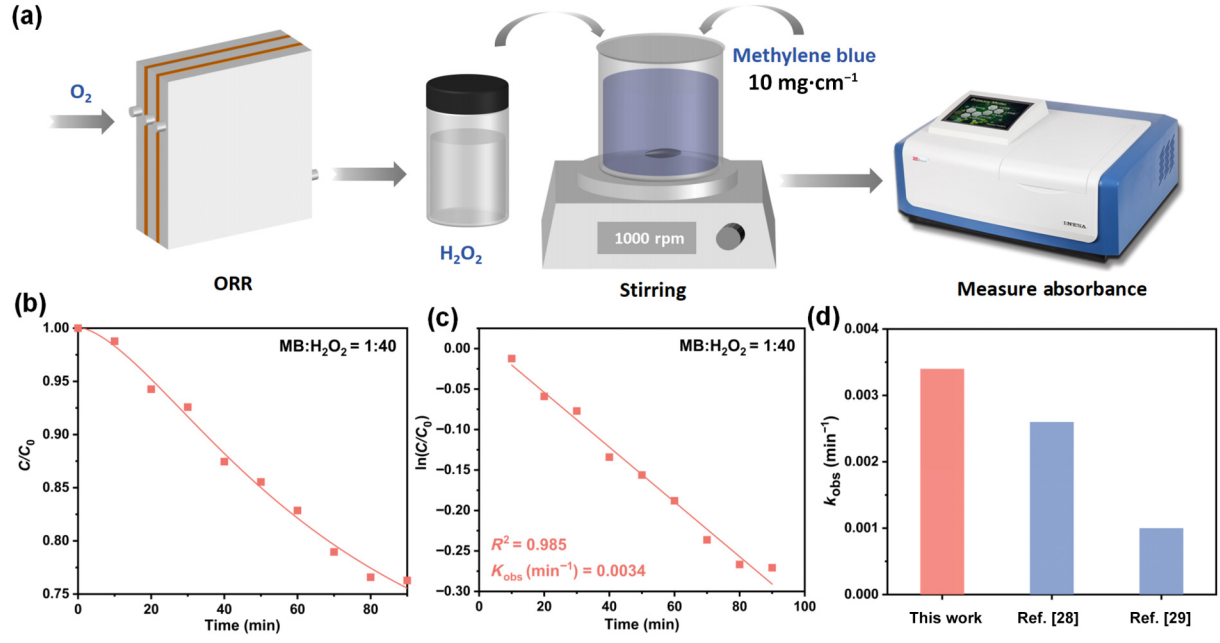

Figure 4 (a) The schematic diagram of the application of the produced H_2O_2 to the pollutant degradation. (b) and (c) Degradation efficiency of MB aqueous solutions by the prepared H_2O_2 (initial dye concentration = 10 mg·L^{-1}, H_2O_2 = 39.6 mM). (d) Comparison of the degradation kinetics of MB using only H_2O_2 in this work and other literature (Ref. [28]: MB:H_2O_2 = 1:80, Ref. [29]: MB:H_2O_2 = 1:200).

the prepared H_2O_2 in practical applications. Assuming application to industrial pollutant degradation, the ORR and pollutant degradation can be realized simultaneously, as long as the O_2 is continuously supplied and the generated H_2O_2 is directly added to the pollutants. Compared with the traditional method of preparing H_2O_2 by the anthraquinone process and then using the prepared H_2O_2 for sewage degradation, this method greatly shortens the overall time and improves the degradation efficiency.

4 Conclusion

In summary, we synthesized a high-dimensional rod-like structure of Nb_2O_5, which demonstrated excellent electrocatalytic performance in the ORR for H_2O_2 production. The FE of H_2O_2 reached as high as 94% at 50 mA·cm^{-2}, and the yield of H_2O_2 achieved 874 mmol·g_{cat}^{-1}·h^{-1}. At an industrial-grade current density (250 mA·cm^{-2}), the FE also reached 90%. After 34 h of stable operation of the ORR of the material, the FE of H_2O_2 is still as high as 76%. The dynamic changes of the catalyst were revealed by *in situ* Raman spectroscopy, and a series of experiments and characterizations confirmed that the NbO_6 octahedra were the key factor contributing to its excellent electrocatalytic performance. The generated H_2O_2 enables rapid degradation of pollutants and has a strong potential for environmental applications. This work deepens the understanding of the structure–performance correlation and presents a novel strategy for advancing high-efficiency and environmentally friendly H_2O_2 electrocatalysts.

Electronic Supplementary Material: Supplementary material (catalyst morphology characterization, Faraday efficiency calculations for H_2O_2 production, measurement of pollutant degradation rate, structural characterization (XRD pattern, Raman spectra, XPS spectra, and SEM images) of Nb_2O_5-HD, electrochemical testing of different crystalline forms of Nb_2O_5, and MB degradation rate at high concentration of H_2O_2) is available in the online version of this article at https://doi.org/10.26599/NR.2025.94907917.

Data availability

All data needed to support the conclusions in the paper are presented in the manuscript and the Electronic Supplementary Material. Additional data related to this paper may be requested from the corresponding author upon request.

Acknowledgements

We acknowledge with gratitude the financial support received from the National Key Research and Development Program of China (No. 2022YFC3703503), the Science and Technology Commission of Shanghai Municipality (No. 24ZR1416000), and Shanghai Municipal Bureau of Ecology and Environment (No. 2025, HUHUANKE No. 35). Our sincere thanks extend to the Japan Society for the Promotion of Science (JSPS) for their generous funding through the Grant-in-Aid for Scientific Research (Nos. 23K26698 and 23K26456). Furthermore, the Joint Usage/Research Center for Catalysis partially contributed to the facilitation of this research.

Declaration of competing interest

All the contributing authors report no conflict of interests in this work.

Author contribution statement

B. X. C.: Writing manuscript, investigation, data curation. X. L. W.: Data curation, formal analysis. S. J. L.: Investigation. Y. H. L.: Methodology. T. M.: Funding acquisition, supervision. T. I.: Supervision. G. L. X.: Project administration, supervision. K. I.: DFT calculation. Y. F. F.: Manuscript verification. Y. N. W.: Manuscript

verification. M. Y. L.: Writing – review & editing, supervision, methodology. All the authors have approved the final manuscript.

Use of AI statement

None.

References

[1] Gu, P.; Zheng, M. B.; Zhao, Q. X.; Xiao, X. G.; Xue, H.; Pang, H. Rechargeable zinc-air batteries: A promising way to green energy. *J. Mater. Chem. A* **2017**, *5*, 7651–7666.

[2] Zhao, R. F.; Huan, L.; Gu, P.; Guo, R.; Chen, M.; Diao, G. W. Yb,Er-doped CeO_2 nanotubes as an assistant layer for photoconversion-enhanced dye-sensitized solar cells. *J. Power Sources* **2016**, *331*, 527–534.

[3] Bu, Y. F.; Wang, Y. B.; Han, G. F.; Zhao, Y. X.; Ge, X. L.; Li, F.; Zhang, Z. H.; Zhong, Q.; Baek, J. B. Carbon-based electrocatalysts for efficient hydrogen peroxide production. *Adv. Mater.* **2021**, *33*, 2103266.

[4] Xu, Z. Q.; Zhao, H. T.; Liang, J.; Wang, Y.; Li, T. S.; Luo, Y. S.; Shi, X. F.; Lu, S. Y.; Feng, Z. S.; Wu Q. et al. P. Noble-metal-free electrospun nanomaterials as electrocatalysts for oxygen reduction reaction. *Mater. Today Phys.* **2020**, *15*, 100280.

[5] Zhang, Y.; Jiang, H.; Zhang, C. X.; Feng, Y. B.; Feng, H.; Zhu, S. Y.; Hu, J. High-efficiency oxygen reduction by late transition metal oxides to produce H_2O_2. *J. Mater. Chem. A* **2024**, *10*, 6123–6133.

[6] Deng, Q. L.; Fu, Y. P.; Zhu, C. B.; Yu, Y. Niobium-based oxides toward advanced electrochemical energy storage: Recent advances and challenges. *Small* **2019**, *15*, 180484.

[7] Pilarek, B.; Pelczarska, A. J.; Szczygieł, I. Characterization of niobium(V) oxide received from different sources. *J. Therm. Anal. Calorim.* **2017**, *130*, 77–83.

[8] Peng, X. G.; Zhang, S. J.; Bao, Z. K.; Ding, L.; Wang, G. L.; Shao, Y. Z.; Xu, Z. X.; Ji, W. K.; Feng, G.; Wang, S. B. et al. Oxygen vacancies on Nb_2O_5 enhanced the performance of H_2O_2 electrosynthesis from O_2 reduction. *Chem. Commun.* **2022**, *58*, 8428–8431.

[9] Peng, X. G.; Bao, Z. K.; Zhang, S. J.; Li, Y. A.; Ding, L.; Shi, H. J.; Liu, J.; Zhong, X.; Li, X. N.; Wang, J. G. Modulation of Lewis and Brønsted acid centers with oxygen vacancies for Nb_2O_5 electrocatalysts: Towards highly efficient simultaneously electrochemical ozone and hydrogen peroxide production. *Chem. Eng. Sci.* **2023**, *271*, 118573.

[10] Murayama, T.; Chen, J. L.; Hirata, J.; Matsumoto, K.; Ueda, W. Hydrothermal synthesis of octahedra-based layered niobium oxide and its catalytic activity as a solid acid. *Catal. Sci. Technol.* **2014**, *4*, 4250–4257.

[11] Ishikawa, S.; Shinoda, M.; Motoki, Y.; Tsurumi, S.; Kimura, M.; Hiyoshi, N.; Yoshida, A.; Ueda, W. Synthesis of fluoride-containing high dimensionally structured Nb oxide and its catalytic performance for acid reactions. *Inorg. Chem.* **2020**, *59*, 9086–9094.

[12] Shimoda, K.; Ishikawa, K.; Tahiro, M.; Kumaki, M.; Hiyoshi, N.; Ueda, W. Synthesis of high dimensionally structure Mo–Fe mixed metal oxide and its catalytic activity for selective oxidation of methanol. *Inorg. Chem.* **2020**, *59*, 5252–5255.

[13] Shimoda, K.; Ishikawa, S.; Matsumoto, K.; Miyasawa, M.; Takebe, M.; Matsumoto, R.; Lee, S.; Ueda, W. Nb–V Mixed oxide with a random assembly of pentagonal units: A catalyst for oxidative dehydrogenation of ethane and propane. *Chem. Cat. Chem.* **2021**, *13*, 3132–3139.

[14] Kreissl, H. T.; Li, M. M. J.; Peng, Y. K.; Nakagawa, K.; Hooper, T. J. N.; Hanna, J. V.; Shepherd, A.; Wu, T. S.; Soo, Y. L.; Tsang, S. C. E. Structural studies of bulk to nanosize niobium oxides with correlation to their acidity. *J. Am. Chem. Soc.* **2017**, *139*, 12670–12680.

[15] Jehng, J. M.; Wachs, I. E. Structural chemistry and Raman spectra of niobium oxides. *Chem. Mater.* **1991**, *3*, 100–107.

[16] Brayner, R.; Bozon-Verduraz, F. Niobium pentoxide prepared by soft chemical routes: Morphology, structure, defects and quantum size effect. *Phys. Chem. Chem. Phys.* **2003**, *5*, 1457–1466.

[17] Zhang, B. B.; Wang, L.; Zhang, Y. J.; Ding, Y.; Bi, Y. P. Ultrathin FeOOH nanolayers with abundant oxygen vacancies on $BiVO_4$ photoanodes for efficient water oxidation. *Angew. Chem., Int. Ed.* **2018**, *57*, 2248–2252.

[18] Anantharaj, S.; Ede, S. R.; Karthick, K.; Sam Sankar, S.; Sangeetha, K.; Karthikc, P. E.; Kundu, S. Precision and correctness in the evaluation of electrocatalytic water splitting: revisiting activity parameters with a critical assessment. *Energy Environ. Sci.* **2018**, *11*, 744–771.

[19] Xia, Y.; Zhao, X. H.; Xia, C.; Wu, Z. Y.; Zhu, P.; Kim, J. Y.; Bai, X. W.; Gao, G. H.; Hu, Y. F.; Zhong, J. et al. Highly active and selective oxygen reduction to H_2O_2 on boron-doped carbon for high production rates. *Nat. Commun.* **2021**, *12*, 4225.

[20] Wang, Y. L.; Shi, R.; Shang, L.; Peng, L. S.; Chu, D. W.; Han, Z. J.; Waterhouse, G. I. N.; Zhang, R.; Zhang, T. R. Vertical graphene array for efficient electrocatalytic reduction of oxygen to hydrogen peroxide. *Nano Energy* **2022**, *96*, 107046.

[21] Zhang, Q. Z.; Zhou, M. H.; Ren, G. B.; Li, Y. W.; Li, Y. C.; Du, X. D. Highly efficient electrosynthesis of hydrogen peroxide on a superhydrophobic three-phase interface by natural air diffusion. *Nat. Commun.* **2020**, *11*, 1731.

[22] Chen, S. Y.; Luo, T.; Chen, K. J.; Lin, Y. Y.; Fu, J. W.; Liu, K.; Cai, C.; Wang, Q. Y.; Li, H. J. W.; Li, X. Q. et al. Chemical identification of catalytically active sites on oxygen-doped carbon nanosheet to decipher the high activity for electro-synthesis hydrogen peroxide. *Angew. Chem., Int. Ed.* **2021**, *60*, 16607–16614.

[23] Oh, J. M.; Venters, C. C.; Di, C.; Pinto, A. M.; Wan, L. L.; Younis, I.; Cai, Z. Q.; Arai, C.; So, B. R.; Duan, J. Q. et al. U1 snRNP regulates cancer cell migration and invasion *in vitro*. *Nat. Commun.* **2020**, *11*, 1.

[24] Zhang, E. H.; Tao, L.; An, J. K.; Zhang, J. W.; Meng, L. Z.; Zheng, X. B.; Wang, Y.; Li, N.; Du, S. X.; Zhang, J. T. et al. Engineering the local atomic environments of indium single-atom catalysts for efficient electrochemical production of hydrogen peroxide. *Angew. Chem., Int. Ed.* **2022**, *61*, e202117347.

[25] Xiao, C. Q.; Cheng, L.; Zhu, Y. H.; Wang, G. C.; Chen, L. Y.; Wang, Y. T.; Chen, R. Z.; Li, Y. H.; Li, C. Z. Super-coordinated nickel $N_4Ni_1O_2$ site single-atom catalyst for selective H_2O_2 electrosynthesis at high current densities. *Angew. Chem., Int. Ed.* **2022**, *61*, e202206544.

[26] Zhang, Y. C.; Afzal, N.; Pan, L.; Zhang, X. W.; Zou, J. J. Structure–activity relationship of defective metal-based photocatalysts for water splitting: Experimental and theoretical perspectives. *Adv. Sci.* **2019**, *6*, 1900053.

[27] Cai, Y.; Li, X.; Wang, L.; Gao, H. Y.; Zhao, Y. N.; Ma, J. M. Oleylamine-assisted hydrothermal synthesis of ultrasmall NbO_x nanoparticles and their *in situ* conversion to NbO_x@C with highly reversible lithium storage. *J. Mater. Chem. A* **2015**, *3*, 1396–1399.

[28] Sugha, A.; Bhatti, M. S. Degradation of methylene blue dye by UV/H_2O_2 advanced oxidation process: Reaction kinetics, residual H_2O_2 and specific energy consumption evaluation. *Desalination Water Treat.* **2022**, *274*, 297–307.

[29] Sukhatskiy, Y.; Sozanskyi, M.; Shepida, M.; Znak, Z.; Gogate, P. R. Decolorization of an aqueous solution of methylene blue using a combination of ultrasound and peroxate process. *Sep. Purif. Technol.* **2022**, *288*, 120651.